Changes in diffusion path length with old age in diffuse optical tomography

Clément Bonnéry
Paul-Olivier Leclerc
Michèle Desjardins
Rick Hoge
Louis Bherer
Philippe Pouliot
Frédéric Lesage

Changes in diffusion path length with old age in diffuse optical tomography

Clément Bonnéry,[a] **Paul-Olivier Leclerc,**[b] **Michèle Desjardins,**[a] **Rick Hoge,**[b] **Louis Bherer,**[c]
Philippe Pouliot,[a,d] **and Frédéric Lesage**[a,d]

[a]Ecole Polytechnique, Department of Electrical Engineering, C.P. 6079, Succursale Centre-ville, Montréal, Quebec, H3C 3A7, Canada
[b]Université de Montréal, Department of Physiology, Quebec, Canada
[c]UQAM, Department of Psychology, Montréal, Quebec, Canada
[d]Montreal Heart Institute, Research center, Quebec, Canada

Abstract. Diffuse, optical near infrared imaging is increasingly being used in various neurocognitive contexts where changes in optical signals are interpreted through activation maps. Statistical population comparison of different age or clinical groups rely on the relative homogeneous distribution of measurements across subjects in order to infer changes in brain function. In the context of an increasing use of diffuse optical imaging with older adult populations, changes in tissue properties and anatomy with age adds additional confounds. Few studies investigated these changes with age. Duncan et al. measured the so-called diffusion path length factor (DPF) in a large population but did not explore beyond the age of 51 after which physiological and anatomical changes are expected to occur [*Pediatr. Res.* 39(5), 889–894 (1996)]. With increasing interest in studying the geriatric population with optical imaging, we studied changes in tissue properties in young and old subjects using both magnetic resonance imaging (MRI)-guided Monte-Carlo simulations and time-domain diffuse optical imaging. Our results, measured in the frontal cortex, show changes in DPF that are smaller than previously measured by Duncan et al. in a younger population. The origin of these changes are studied using simulations and experimental measures. © *2012 Society of Photo-Optical Instrumentation Engineers (SPIE).* [DOI: 10.1117/1.JBO.17.5.056002]

Keywords: diffuse optical tomography; aging; time-domain optical imaging; magnetic resonance imaging.

Paper 12013 received Jan. 6, 2012; revised manuscript received Mar. 5, 2012; accepted for publication Mar. 7, 2012; published online May 4, 2012.

1 Introduction

Diffuse optical imaging is a brain imaging technique used to study the temporal and spatial neuronal activity in the brain.[1] Near infrared spectroscopy takes advantages of light absorption in the tissue of interest, which is dominated by water, oxy- and deoxyhemoglobin in the near infrared, and can be linearly linked to changes in chromophore concentrations. In continuous-wave near infrared spectroscopy (CW-NIRS), continuous monochromatic light emitted by sources located at the surface of the scalp, is both scattered and absorbed by cortical tissues and superficial tissue layers so that changes in measured intensities can provide information about cerebral hemodynamics from surface measurements. However, due to its inability to separate absorption and scattering and to provide absolute measures of optical parameters, CW-NIRS is unable to generate quantitative values of hemoglobin concentrations.[2] Thus assumptions are required about tissue properties.

As with other hemodynamic techniques, neuronal activation is indirectly monitored through the neurovascular coupling.[3] Following neuronal activity, possibly due to local information processing, a local hemodynamic response occurs enhancing the supply in oxyhemoglobin and glucose and the removal of carbon dioxide. The hypothesis of linearity between neural and hemodynamic changes, associated with accurate measures of the latter can be used to generate activation maps, akin to the ones developed in functional magnetic resonance imaging

(fMRI).[4] Recent work toward robust statistical parametric mapping for near infrared spectroscopy (NIRS) provided a framework to compare groups and populations based on measured responses.[5] Further advances using multimodality to provide anatomical a priori information extended early topographical studies to three-dimensional (3-D) tomographic reconstruction of activity in both space and time.[6,7]

These progresses in data analysis, the instruments, portability, flexibility, and minimal invasiveness led to increased interest in finding clinical scenarios where CW-NIRS could be applied. The elderly population presents easy access to the brain as they have pale or even no hair and benefit from the noninvasiveness of the technique. For example, in the context of cognition and aging neuroscience studies, CW-NIRS has been used to investigate focalisation and lateralization of brain activity.[8–11]

However, with aging, changes in the measured hemodynamic response and associated activation maps are related to changes in neuronal processing but also to modifications of physiology with age. There is evidence that cerebral blood flow and cerebral oxygenation decrease[12,13] and that the capability to respond to strong demands in oxygen declines with age.[14] Leveque et al. proposed the idea that capillary circulation significantly decreases in the skin around 60 years causing the strong changes in light propagation properties in skin observed at the same age.[15] Other changes associated with the process of normal aging are associated with anatomy: Bones become more porous,[16] whereas elasticity properties of the skin decline. Both have decreasing thicknesses even if there is no consensus

Address all correspondence to: Frédéric Lesage, C.P. 6079 Succursale Centre-ville, Montréal, Québec, Canada. Tel: +1 5143404711; Fax: +1 5143404611; E-mail: frederic.lesage@polymtl.ca

about the onset age from which this phenomena affects the skin. Some authors claim the onset age to be around 45 years.[15]

The above changes in the properties of tissues and how they interact with light may affect CW-NIRS observations. Whereas long term/lifetime evolution of light absorption is of interest since it contains information about hemodynamics, changes in the diffusion properties can bias measurements and ensuing statistical analyses comparing young and old populations. The simplest formulation to characterize these changes is the modified Beer Lambert law, Eq. (1), where d is the distance separating the source and the detector, I/I_0 describe the intensity changes with respect to baseline, $\Delta\mu_a(\lambda)$ the associated change in absorption (at illumination wavelength λ), and $D(\lambda)$ the differential pathlength factor, i.e., the term correcting the pathlength value so that the Beer-Lambert law can be applied to turbid media such as biological tissues:

$$I/I_0 = \exp[-dD(\lambda)\Delta\mu_a(\lambda)]. \tag{1}$$

Formally, the coefficient $D(\lambda)$ is defined as a function of $\langle \bar{L} \rangle$, the mean average path length of detected photons over the range of absorption coefficient from μ_{a0} to $\mu_{a0} + \Delta\mu_a$.[17]

$$D(\lambda) \stackrel{\text{def}}{=} \frac{\langle \bar{L} \rangle}{d} \quad \text{with} \quad \langle \bar{L} \rangle = \frac{1}{\Delta\mu_a} \int_{\mu_{a0}}^{\mu_{a0}+\Delta\mu_a} \langle L \rangle d\mu_a'. \tag{2}$$

Equation (2) shows that $D(\lambda)$ depends on a large number of parameters: heterogeneity of the tissues, scattering and absorption coefficients which are dependent on the anatomy, and the local tissue hemoglobin concentration. Other important factors influencing the diffusion path length factor (DPF) are the wavelength and source-detector distance since both will impact where detected photons will travel.

A power law between the DPF and the age of the subjects ranging from 1 day old to 50 years old has been empirically established previously by Duncan et al.[18] using intensity modulated optical spectrophotometer measurements in 283 subjects. In that work, the setup consisted of a single source and detector pair placed on the left side of the forehead just below the hairline (for adults). Even if Duncan et al. specified that DPF estimations showed important variation among subjects belonging to the same age bin, the high repeatability of the measures on the forearm – 0.8% – has won unanimity among the NIRS community. However, by current standards, the oldest subjects acquired in this study remain young. Changes in anatomy and physiology described above with aging are expected to appear later in life and measured data evaluating the DPF in older subjects is lacking. Assessing the validity of the power law beyond 50 years is required in view of the increasing number of NIRS aging studies.

A separate question is to identify the main causes for the observed changes in the DPF. Several studies have demonstrated the prominence of the cerebrospinal fluid (CSF) layer in modulating the value of the DPF. With Monte Carlo simulations and experiments on phantoms, Okada et al.[19] have shown a large influence of CSF on the DPF estimations in both simulations and in measures. The specific impact of the value of the reduced scattering coefficient, μ_s', in that layer has also been studied. As long as the inverse of the coefficient was larger than the average thickness of the CSF layer, its value did not have a large influence on the results as was demonstrated with Monte Carlo simulations.[20] However, the CSF thickness is variable around the head. As a result the position of sources and detectors is of

prime importance as are source-detector distances.[19,20] Observations show that the DPF increases until source-detector distances reach about 2.5 cm where they reach a plateau. In contradistinction, sulci geometry and gray and white matter boundaries are not expected to have much influence on the DPF.[19] Thus measuring the DPF at a number of source-detector distances may be required for accuracy.

With aging, two main factors are expected to modulate the DPF. First, the morphology changes, e.g., brain shrinkage,[21,22] will impact measures. Second, changes in skin and skull optical properties are also expected to modulate the DPF. The high variability of the DPF among subjects of the same age supports the hypothesis that morphology and optode placement have a key role. Our primary goal in this work was to extend Duncan et al.'s[18] findings and measure the DPF between 60 and 70 years of age, contributing experimental data to support aging NIRS studies. This was performed using two methods: simulations and time-domain measures. Realistic head models using individual anatomical magnetic resonance images (MRIs) and Monte-Carlo simulations were used to evaluate the impact of layer geometry on DPF changes. Separately, measures using time resolved spectroscopy acquisitions (TRS) at multi-distances were performed. Additional simulations to test the influence of layer thickness (other than CSF) and optical coefficients on phantoms were also done. Results confirm a slight increase of the DPF with age, showing that Duncan's result can be extended to older adults. We also show a larger dependence of these estimations on optical coefficients than on geometry.

2 Methodology

Forty-three healthy adult right-handed volunteers participated in this study, divided in two age groups: 19 young adults (age 24.4 ± 2.5, 10 females) and 23 older adults (age 67.6 ± 2.9, 17 females). In either age group, there was no significant difference between the ages of the males compared to those of the females (2-sampled t-test, $P > 0.1$). Exclusion criteria included any history of neurological, cardiovascular or respiratory disease, color-blindness, functional analphabetism, smoking, drug or alcohol problem, signs of early dementia as assessed by the Mini-Mental State Examination, and any serious contraindication to MR imaging. This study was approved by the institutional review board of the Unité de Neuroimagerie Fonctionnelle of the Center de Recherche de l'Institut Universitaire de Gériatrie de Montréal (UNF/CRIUGM) and that of École Polytechnique de Montréal. Written consent was obtained from all subjects prior to the study. Subjects underwent two tests on the same day described in the next sections.

2.1 Time Resolved Spectroscopy

The TRS system consisted of four pulsed lasers operating at 690, 750, 800, and 850 nm and four single-photon counting avalanche detectors (SPADs). Whereas all four lasers were illuminating the same optical fiber, each of the SPADs were connected to a distinct fiber used to collect light. As shown in Fig. 1, the source and the four detection fibers were fastened to a rubber patch placed on the left side of the forehead of each subject. The source was positioned above the Fp1 point of the 10 to 20 system. Source-detector distances were, respectively 10, 15, 25, and 30 mm.

The experiment took place in a dark room to reduce the SPADs noise. The subjects were seated on a comfortable chair and were asked to stay calm during the acquisition.
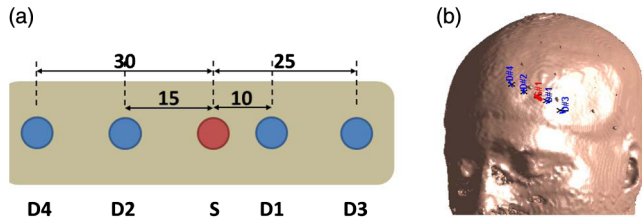
(a)

(b)

Fig. 1 Diagram of the TRS rubber patch (a) and its positioning on one of the study subjects (b). Source-detector distances specified in millimeters.

Photons were collected for a period of 5 min to generate sufficient statistics. The fitting procedure used a nonlinear optimization routine (MATLAB function lsqcurvefit) with parameters μ_a, μ_s', and an amplitude factor to get the best fit of the theoretical model for a homogeneous medium to the experimental temporal point spread functions (TPSFs). The 16 TPSFs (four distances times four wavelengths) were fit individually with a homogeneous model with the same three parameters: μ_a, μ_s', and the amplitude factor.

To extract optical parameters (μ_a, μ_s') for each wavelength, each theoretical TPSF function of the medium was convolved with the experimental instrument response function (IRF) before comparison with the experimental TPSF. Finally, hemoglobin concentrations were recovered by inverting Eq. (3) with a least-square fit for the only layer of this homogeneous model. We assumed that tissues contained 70% water.

$$\begin{bmatrix} \mu_a(\lambda_1) \\ \mu_a(\lambda_2) \\ \mu_a(\lambda_3) \\ \mu_a(\lambda_4) \end{bmatrix} = \begin{bmatrix} \epsilon_{HbO_2}^{\lambda_1} & \epsilon_{HbR}^{\lambda_1} & \epsilon_{H_2O}^{\lambda_1} \\ \epsilon_{HbO_2}^{\lambda_2} & \epsilon_{HbR}^{\lambda_2} & \epsilon_{H_2O}^{\lambda_2} \\ \epsilon_{HbO_2}^{\lambda_3} & \epsilon_{HbR}^{\lambda_3} & \epsilon_{H_2O}^{\lambda_3} \\ \epsilon_{HbO_2}^{\lambda_4} & \epsilon_{HbR}^{\lambda_4} & \epsilon_{H_2O}^{\lambda_4} \end{bmatrix} \begin{bmatrix} C_{HbO_2} \\ C_{HbR} \\ C_{H_2O} \end{bmatrix}. \quad (3)$$

The following formula from[23] was used to compute the DPF from TRS:

$$D(\lambda) = \frac{1}{2}\left(3\frac{\mu_s'}{\mu_a}\right)^2 \left[1 + \frac{1}{d(3\mu_s'\mu_a)^{1/2}}\right]^{-1}. \quad (4)$$

2.2 Magnetic Resonance Imaging

The data was acquired on a Siemens Trio 3T system. The anatomical image was a T1-weighted MPRAGE sequence with isotropic resolution of 1 mm^3 on a 256×256 matrix, TE/TR/FA = 2.98 ms/2300 ms/9 deg. For the young adults ($N = 19$), an iPAT GRAPPA acceleration factor of two was used to decrease acquisition time.

2.3 Monte Carlo Simulations

2.3.1 Simulations on phantoms

A numerical phantom consisting of a planar-parallel volume with five layers was designed. The following set of layers' thicknesses was used as reference: 5 mm for scalp, 5 mm for skull, 2 mm for CSF, and 4 mm for gray matter. Those values were chosen since they were the reference case[19] and were in the ranges of values provided by our measurement technique (Sec. 2.3.2).

This simplified phantom had three purposes. First, it was used to assess the accuracy of the Monte-Carlo based thickness measurements described below. Second, layer thicknesses in the phantom associated with CSF, skull, and scalp were successively changed to evaluate the effect of each layer thickness on the DPF. The thickness of the CSF, skull or scalp was changed while other layers were kept unchanged to generate a total of eleven different configurations. Finally, preliminary tests were run to evaluate the number of photons required in simulations so that the variance in DPF between different simulations on the same phantom was kept low. Simulations showed that with 10^7 launched photons, the DPF variance was below 1%. In the simulations below, 2×10^7 photons were launched, and an average of $3 \times 10^4 \pm 2 \times 10^3$ photons were detected.

2.3.2 Simulations on individual subject heads

NIRS10 toolbox and simulations. The forward light propagation model used individual anatomical T1 images. The MRI images were first processed by SPM8.[4] Tissue segmentations were done with the NewSegment toolbox and a home-made SPM-compatible toolbox hereafter referred to as NIRS10 (available upon request). The latter SPM toolbox was developed to process CW-NIRS data in the context of multimodal studies. Five tissues and air were segmented: gray and white matter, CSF, skull, and scalp. While air is not a tissue, its low scattering properties were taken into account since simulations were done near the paranasal sinuses. To generate a measurement geometry in simulations, the neuronavigation system Brainsight (Rogue Research Inc., Montréal, Canada) was used to align T1 images from MRI and the patch holding the optical fibers for the TRS measurements in one subject. These positions were then mapped in normalized brain coordinates (using the MNI template), and positions of the source and detectors on each T1 subject images were then obtained after applying the nonlinear transformation linking normalized and subject spaces.

The code Monte Carlo eXtreme (MCX)[24] was chosen to run the simulations. The code computes the partial pathlength followed by each photon in each layer of the head for a given detector. Moreover, it also provides the number of scattering events that each photon undergoes throughout its path inside the head. The method proposed by Hiraoka et al.[25] was then used to compute the DPF for each of the four source-detector pairs. The optical parameters used for simulations are provided in Table 1.

Thickness measurements. An estimate of layers' thicknesses was obtained from the history files recording the pathlengths for each detected photon. For this, a separate

Table 1 Absorption and scattering coefficients (mm^{-1}) from literature[26] used in Monte-Carlo simulations. Anisotropy was fixed to 0.9 in all layers and refraction index to 1.4.

		Scalp	Skull	CSF	GM	WM
690 nm	μ_a	0.0162	0.0103	0.0004	0.0182	0.0182
	μ_s	7.87	9.83	0.10	12.29	12.29
830 nm	μ_a	0.0199	0.0141	0.0026	0.0193	0.0193
	μ_s	6.47	8.43	0.10	10.88	10.88

simulation was done where the anisotropy and the absorption coefficient were set to zero, while the reduced scattering coefficient was decreased to 0.005 in scalp, skull, gray, and white matter. The source and the four detectors were considered successively as simulation photon sources. For each simulation, one voxel of white matter situated along the normal axis of the simulation source was changed into air so that MCX registered photons going through this particular voxel. Only photons which did not undergo any scattering events were considered for this measure. The recorded partial pathlengths were then used as a proxy for the respective thicknesses of the scalp, skull, and CSF layers. While indirect, this measure facilitated uniform evaluation of layer thickness across subjects without subjective human interaction. It was validated in the phantoms above and found to be accurate.

3 Results

3.1 Effect of Layer Thickness on Monte Carlo Simulations

The five layer phantom is presented in Fig. 2(a), and Monte-Carlo based DPF estimations were done for both 10 mm and 30 mm source-detector distances. Figure 2(b) shows the effect of CSF thickness when varied between 1 and 4 mm with $\mu_s' = 0.1$ mm. Figure 2(c) and 2(d) shows, respectively the impact of the most superficial layers (scalp and skull) on the DPF as their thicknesses varied from 3 to 6 mm.

Results showed an increase in the estimated DPF of the 30 mm distance channel with the thickening of scalp or skull but no significant effect with changes in CSF thickness (mean DPF 6.14 ± 0.02 for 690 nm and 5.24 ± 0.03 for 830 nm over the thickness range 1 to 5 mm). With a source detector separation of 10 mm, the DPF was observed to be less sensitive to layer

thickness. For this distance, the averaged largest difference in the DPF had a mean of 0.045 ± 0.003 for 690 nm and 0.032 ± 0.014 for 830 nm. These results show that with respect to changes in thickness, the longer distance pairs were more sensitive, while the short distance pairs saw small changes as the DPF values were dominated by the first layer.

3.2 Effect of Source or Detector Positions on Monte Carlo Simulations

To assess the impact of optode positioning errors on simulations in realistic geometries, we computed DPF on all subjects by introducing an offset of 1 cm to translate the probe toward the right or the top of the head. Group results are shown in Fig. 3 for 690 nm and in Fig. 4 for 830 nm. No significant change was found between the different positions at 690 nm or 830 nm despite mean DPF variations reaching 14%.

3.3 Estimation of Layer Thickness with Respect to Age

Layer thickness estimations from Monte-Carlo following the procedure described in Sec. 2.3.2 were performed in the layered phantom and confirmed the reliability of this method with a simple geometry. The same procedure was thus used with T1 segmented images. Computed layer thicknesses were then averaged over all subjects and fiber positions. Figure 5(a) displays the averaged layer thicknesses of the first three layers (CSF, skull, and scalp) over all fibers positions in young and old adults. The largest range was found for the CSF layer in older adults due to increased inaccuracies in CSF segmentation. Two sample t-tests indicated no significant difference between young and old groups. However, the comparison of the average values indicated that on average, the
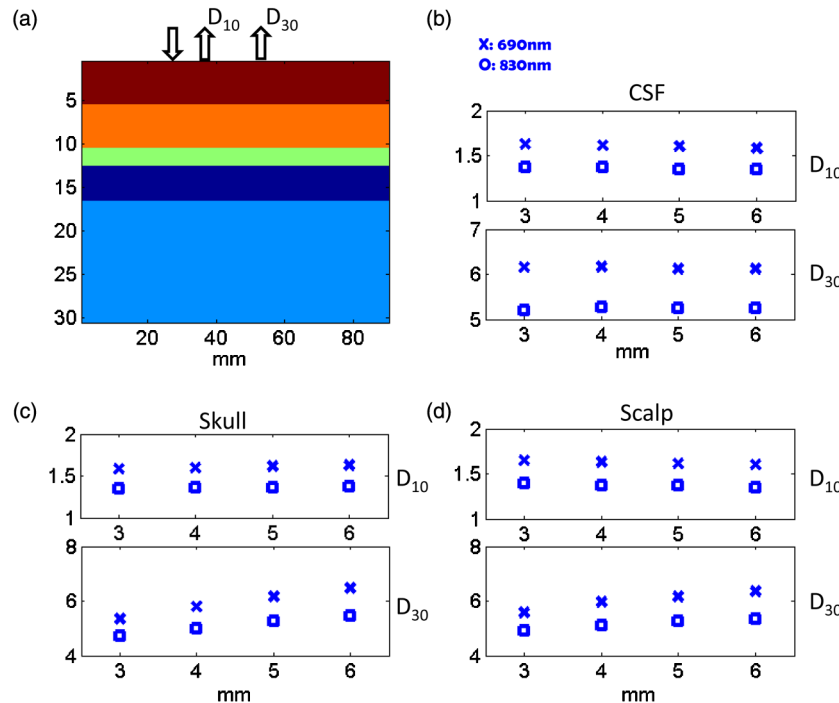

Fig. 2 (a) Reference phantom used for simulations, (b) effect of changes in CSF thickness (1 to 4 mm) on the DPF and (c), (d) effects of skull and scalp thicknesses, respectively (3 to 6 mm) on the DPF. In (b–d), the top panels show results for the 10 mm source-detector distance, the bottom panel for the 30 mm pair. DPFs were computed for 690 nm (crosses) and 830 nm (squares).
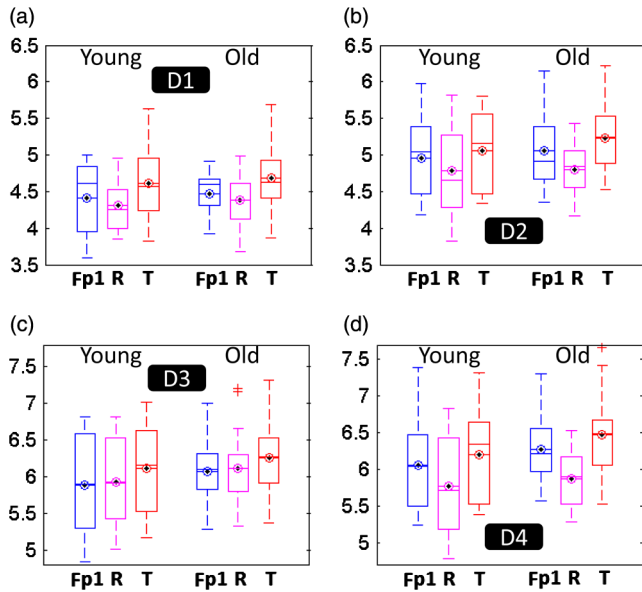
Fig. 3 DPF at 690 nm for groups of young (left side of each subfigure) and old adult (right side of each subfigure) groups with Fp1 positioning (Fp1), offset to the right (R) or to the top (T) for each source-detector pairs S-D1(a), S-D2(b), S-D3(c), S-D4(d). Boxes extend to the first and third quartiles, central horizontal lines are the medians, whereas the eyes represent means. Outliers are represented as crosses.

brain was situated deeper from the surface of the head in the elderly population.

3.4 DPF Change with Age

DPF estimates were computed both from measured data and from Monte-Carlo simulations based on individual MRI images. The rationale for this was to evaluate whether Monte-Carlo
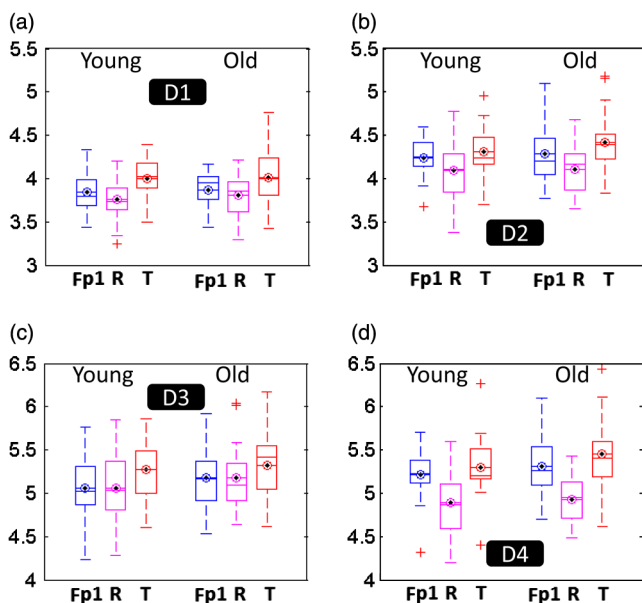

Fig. 4 DPF at 830 nm for groups of young (left side of each subfigure) and old adults (right side of each subfigure) groups with Fp1 positioning (Fp1), offset to the right (R) or to the top (T) for each source-detector pairs S-D1(a), S-D2(b), S-D3(c), S-D4(d). Boxes extend to the first and third quartiles, central horizontal lines are the medians, whereas the eyes represent means. Outliers are represented as crosses.

based estimations scaled with measurements which would form a basis for ongoing work in image reconstruction. A typical Monte-Carlo simulation is shown in Fig. 6.

A similar simulation was done for all subjects and source/detector positions resulting in a total of $N = 4 \times 42 = 168$ simulations per wavelength. Optical parameters used for these simulations are provided in Table 1. Figures 7 (690 nm) and 8 (830 nm) show the estimated values of DPF for all source-detector distances (S-D3) for both the TRS measurements and the estimations performed with Monte-Carlo simulations. The variability observed in Monte-Carlo simulations is not due to simulation statistics, but rather, to realistic differences between subjects' anatomies. In measured data, variability originates from anatomy, optical property, and measurement errors (estimated at 5% in test-retest experiments on phantoms). In the case of the largest source-detector distance [Figs. 7(d) and 8(d)], results found by the heuristic formula developed by Duncan et al.[18] is also overlaid on the data. Since the latter formula was found with a range ending at 50 years, we extrapolated above this age for the older subjects.

DPF evaluated with simulations were lower for both wavelengths and age when compared to TRS measurements or Duncan's values. A two sample t-test showed that the difference between Monte-Carlo and TRS measurements was significant ($P < 0.05$) except for the young subjects measured at 690 nm on the two largest source-detector distances. This underestimation remained even when correcting literature values for measured baseline values of μ_a and μ_s' (a scaling of all optical parameters for each layer was done in proportion with the individual measured homogeneous data values). The offset was smaller with 690 nm than with 830 nm. Averaging over all young and old adults showed that simulated DPF estimates increased slightly. TRS measures showed a larger increase with age but not in the range proposed by Duncan et al.[18] signalling a potential plateau effect in older adults. Two sample t-tests were carried out on young versus old' adults DPF. Results showed no significant difference confirming the variability previously observed in Duncan et al. but p values were seen to decrease with increasing source detector separation.

Finally, to validate the hypothesis that the individual anatomy was the main driver of the observed variability in the DPF, we computed in each case the value of the DPF as a function of the thickness of the first two layers (skin and skull) which were shown in simulations to affect the DPF. Table 2 shows the sum of standard errors (SSE) resulting from a linear regression between the thickness of the first two layers and the DPF. Results showed that more than 90% of the variability could not be explained by thickness changes suggesting that optical parameter changes were more likely to drive DPF values. Using individual parameters in Monte-Carlo simulations confirmed this observation by increasing the residual variability while the simulation using literature optical properties[26] (which only accounts for anatomy changes) showed very high correlation between DPF and the first two layers thickness. While using individual optical parameters increased the variability, providing some indication that it is a cause of DPF changes, an ANOVA analysis did not confirm that the increased variance was better explained by the model with measured values of optical parameters. This may be due to the proportional redistribution of individual measured optical parameters (μ_a, μ_s') to all layers in the absence of a clear procedure to set tissue optical properties from measurements.
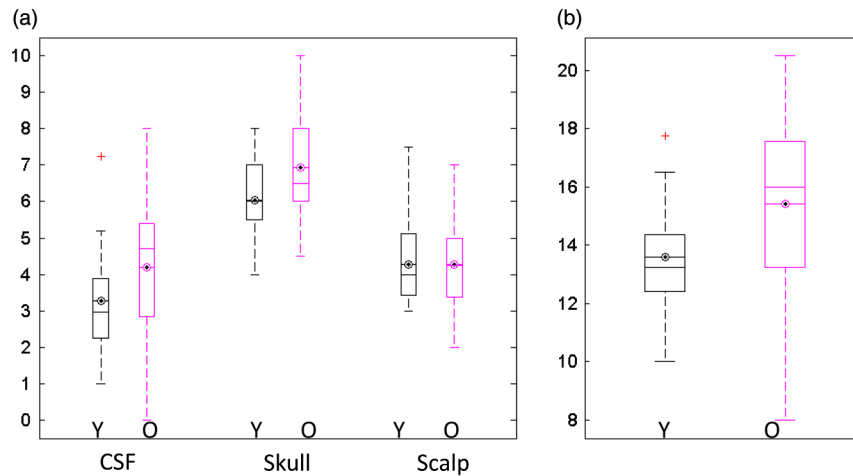
Fig. 5 (a) Computed thicknesses of CSF, Skull and Scalp below the source and four detectors on the TRS patch for young (y) and old adults (o). (b) These three thicknesses have been summed to obtain the depth of the brain inside the head for young (y) and old adults (o). Boxes extend to the first and third quartiles, central horizontal lines are the medians whereas the eyes represent means.
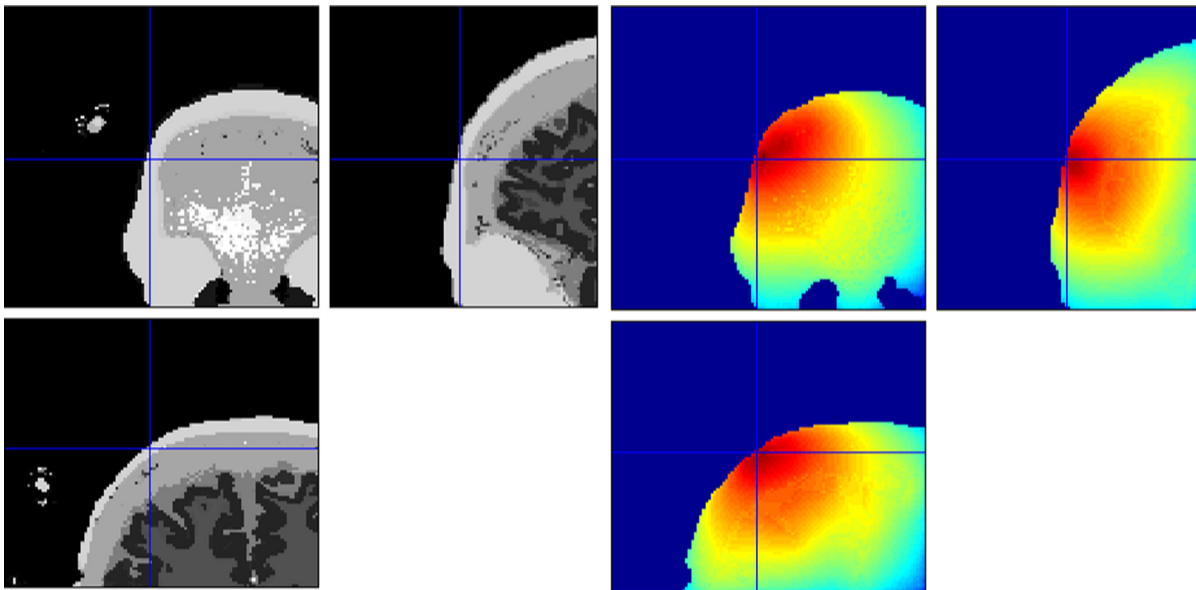

Fig. 6 Monte-Carlo simulation in individual anatomy. Sensitivity matrix is displayed on the right whereas the corresponding segmented anatomical image is on the left.

4 Discussion

This work measured DPFs in young and older adults using time-domain optical imaging and provided for the first time values of the DPF for a population over 51 years of age. Despite documented evidence on anatomical changes of the brain and modifications in physiology and tissue optical properties, our data did not show significant deviations from the empirical law derived by Duncan et al.[18] We observed a lower increase in the DPF than what was expected from the empirical law but high variability in our data did not allow to disprove it. This work thus confirms that extrapolating the empirical law in older populations is possible and can be expected to yield correct results.

Simulations showed that the main geometrical determinants of the DPF were mainly the first two layers of tissue: skin and skull. Clear changes were observed in Monte-Carlo estimations of the DPF with the thickness of those layers in long source-detector pairs. In short source detector pairs, very small variations were observed. In experimental measures, short pairs did indeed show a small change with age suggesting a low dependence on layers thickness. However, in all pairs, experimental measures displayed a large intra-group variability (young versus old) which could not be explained by changes in anatomy. Indeed, when performing Monte-Carlo simulations with literature values of optical properties, the variability of the DPF across our anatomical scans was much lower than measured with TRS suggesting that anatomy alone is not sufficient to explain the large variability in the data. Potential errors could originate from inaccurate segmentations but this would be expected to increase, not decrease variability. We performed separate simulations to test whether using scaled individual optical parameters would explain the variance observed in the data. It was observed that part of the increased variance was explained by the optical parameters, however, a clear procedure to choose how to scale
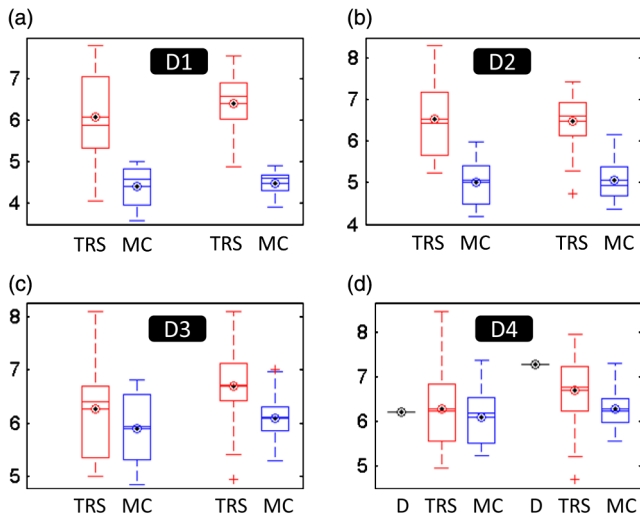
Fig. 7 DPF at 690 nm measured with TRS (TRS), Monte Carlo simulations (MC) for each source-detector pairs S-D1(a), S-D2(b), S-D3(c), S-D4(d) for young (left side of each subfigure) and old adults (right side of each subfigure). Values proposed by Duncan et al.[18] with a source-detector distance of 4.5 cm (d) are also displayed with the TRS largest source-detector pair (d). The boxes extend to the first and third quartiles, central horizontal lines are the medians whereas the eyes represent means.

each optical parameter in each layer would be required to generate precise results. The results however still suggests that changes in optical properties were the main determinant of the variability observed in values of the DPF. As a result, vascularization, pigmentation, and other factors are potentially larger causes of DPF changes than the anatomy.

The high variability of the DPF and the fact that it is left unexplained by an accurate depiction of the anatomy raises questions about the accuracy of tomography techniques. Our Monte-Carlo simulations which are expected to be accurate
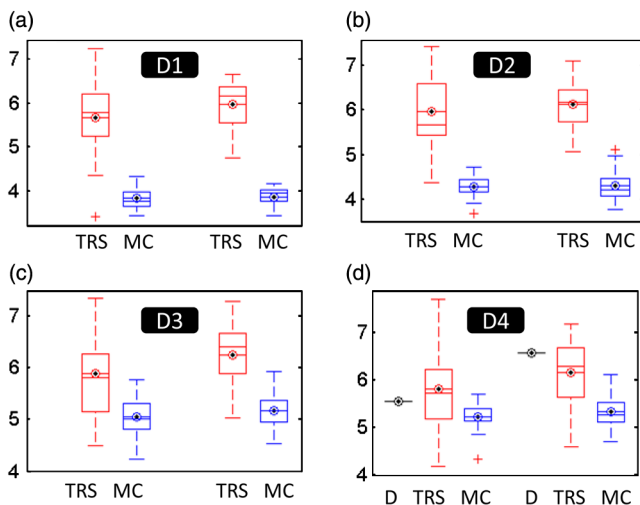

Fig. 8 DPF at 830 nm measured with TRS (TRS), Monte Carlo simulations (MC) for each source-detector pairs S-D1(a), S-D2(b), S-D3(c), S-D4(d) for young (left side of each subfigure) and old adults (right side of each subfigure) groups. Values proposed by Duncan et al.[18] with a source-detector distance of 4.5 cm (d) are also displayed with the TRS largest source-detector pair (d). The boxes extend to the first and third quartiles, central horizontal lines are the medians whereas the eyes represent means.

Table 2 Sum of squares due to error of linear regression of the DPF with respect to thickness of both skin and skull for 30 mm pair.

	690 nm	830 nm
TRS	15.56	12.62
Monte-Carlo: measured optical properties	3.92	2.79
Monte-Carlo: literature optical properties[26]	1.04	0.78

did not explain the changes observed in the data and also systematically provided much lower values of DPF. A statistical test confirmed that result ($P < 0.05$) except for young subjects measured at 690 nm on the two largest source-detector distances. Using Monte-Carlo based reconstructions and literature values of optical properties, even with a correct anatomy, it was shown here to lead to systematic bias in the estimation of a simple measure, the DPF. The systematically lower values may result from literature values being biased with respect to real tissue values. How this bias will translate in studies of brain activation remains to be evaluated. Combining MRI and optical imaging simultaneously may yield some answers to these systematic biases.

A limitation of this study is the fact that optical parameters were computed using a homogeneous model when estimated from TRS data. We previously used a two layer model to estimate parameters from the combined skin-skull-CSF first layer and a second brain layer.[27] Since our simulations showed that the first two layers (skin and skull) were the most important and that the two layer model would be unable to distinguish optical properties for these layers, we found the more stable homogeneous fits to be a better choice. It also allowed a direct comparison with the work of Duncan et al.[18]

5 Conclusion

In this work we extended the range of a previously measured empirical law for the diffusion pathlength factor and studied the main determinants of the variability of DPF in a population of young and old subjects. The results underline the difficulty in explaining measured data in the absence of measures for each tissue layer's optical properties, even with accurate light propagation models. It suggests a cautious approach to image reconstruction techniques associated with NIRS brain imaging.

References

1. E. Gratton et al., "Measurement of brain activity by near-infrared light," *J. Biomed. Opt.* **10**(1) 011008 (2005).
2. D. A. Boas et al., "The accuracy of near infrared spectroscopy and imaging during focal changes in cerebral hemodynamics," *NeuroImage* **13**(1) 76–90 (2001).
3. A. Villringer and U. Dirnagl, "Coupling of brain activity and cerebral blood flow: basis of functional neuroimaging," *Cerebrovasc. Brain Metab. Rev.* **7**(3), 240–276 (1995).

4. W. Penny et al., Eds., *Statistical Parametric Mapping—The Analysis of Functional Brain Images*, 1st ed., Elsevier Ltd. Academic Press, London (2007).

5. J. C. Ye et al., "NIRS-SPM: statistical parametric mapping for near-infrared spectroscopy," *NeuroImage* **44**(2), 428–447 (2009).

6. F. Abdelnour, C. Genovese, and T. Huppert, "Hierarchical bayesian regularization of reconstructions for diffuse optical tomography using multiple priors," *Biomed. Opt. Express* **1**(4), 1084–1103 (2010).

7. F. Abdelnour, B. Schmidt, and T. J. Huppert, "Topographic localization of brain activation in diffuse optical imaging using spherical wavelets," *Phys. Med. Biol.* **54**(20), 6383–6413 (2009).

8. T. Schulte et al., "Age-related reorganization of functional networks for successful conflict resolution: a combined functional and structural MRI study," *Neurobiol. Aging* **32**(11), 2075–2090 (Nov 2011).

9. R. S. Prakash et al., "Age-related differences in the involvement of the prefrontal cortex in attentional control," *Brain Cognit.* **71**(3), 328–335 (2009).

10. R. Cabeza et al., "Aging gracefully: compensatory brain activity in high-performing older adults," *NeuroImage* **17**(3), 1394–1402 (2002).

11. R. Cabeza, "Hemispheric asymmetry reduction in older adults: the HAROLD model," *Psychol. Aging* **17**(1), 85–100 (2002).

12. B. M. Ances et al., "Effects of aging on cerebral blood flow, oxygen metabolism, and blood oxygenation level dependent responses to visual stimulation," *Hum. Brain Mapp.* **30**(4), 1120–1132 (2009).

13. M. Bentourkia et al., "Comparison of regional cerebral blood flow and glucose metabolism in the normal brain: effect of aging," *J. Neurol. Sci.* **181**(1–2), 19–28 (2000).

14. D. J. Mehagnoul-Schipper et al., "Simultaneous measurements of cerebral oxygenation changes during brain activation by near-infrared spectroscopy and functional magnetic resonance imaging in healthy young and elderly subjects," *Hum. Brain Mapp.* **16**(1), 14–23 (2002).

15. J. L. Leveque et al., "In vivo studies of the evolution of physical properties of the human skin with age," *Int. J. Dermatol.* **23**(5), 322–329 (1984).

16. J. Dequeker, "Bone and ageing," *Ann. Rheum. Dis.* **34**(1), 100–115 (1975).

17. A. Sassaroli and S. Fantini, "Comment on the modified beer-lambert law for scattering media," *Phys. Med. Biol.* **49**(14), N255–N257 (2004).

18. A. Duncan et al., "Measurement of cranial optical path length as a function of age using phase resolved near infrared spectroscopy," *Pediatr. Res.* **39**(5), 889–894 (1996).

19. E. Okada et al., "Theoretical and experimental investigation of near-infrared light propagation in a model of the adult head," *Appl. Opt.* **36**(1), 21–31 (1997).

20. A. Custo et al., "Effective scattering coefficient of the cerebral spinal fluid in adult head models for diffuse optical imaging," *Appl. Opt.* **45**(19), 4747–4755 (2006).

21. A. Giorgio et al., "Age-related changes in grey and white matter structure throughout adulthood," *NeuroImage* **51**(3), 943–951 (2010).

22. D. H. Salat et al., "Thinning of the cerebral cortex in aging," *Cerebr. Cortex* **14**(7), 721–730 (2004).

23. J. Choi et al., "Noninvasive determination of the optical properties of adult brain: near-infrared spectroscopy approach," *J. Biomed. Opt.* **9**(1), 221–229 (2004).

24. Q. Fang and D. A. Boas, "Monte carlo simulation of photon migration in 3d turbid media accelerated by graphics processing units," *Opt. Express* **17**(22), 20178–20190 (2009).

25. M. Hiraoka et al., "A monte carlo investigation of optical pathlength in inhomogeneous tissue and its application to near-infrared spectroscopy," *Phys. Med. Biol.* **38**(12), 1859–1876 (1993).

26. G. Strangman, M. A. Franceschini, and D. A. Boas, "Factors affecting the accuracy of near-infrared spectroscopy concentration calculations for focal changes in oxygenation parameters," *NeuroImage* **18**(4), 865–879 (2003).

27. L. Gagnon et al., "Double-layer estimation of intra- and extracerebral hemoglobin concentration with a time-resolved system," *J. Biomed. Opt.* **13**(5), 054019 (2008).